



Ballistic performance of UHMWPE laminated plates and UHMWPE encapsulated aluminum structures: Numerical simulation



Rui Zhang^{a,b,e}, Lu-Sheng Qiang^{b,c}, Bin Han^d, Zhen-Yu Zhao^{b,c}, Qian-Cheng Zhang^e, Chang-Ye Ni^{b,c,*}, Tian Jian Lu^{b,c,*}

^a School of Aerospace, Xi'an Jiaotong University, Xi'an 710049, China

^b State Key Laboratory of Mechanics and Control of Mechanical Structures, Nanjing University of Aeronautics and Astronautics, Nanjing 210016, PR China

^c Nanjing Center for Multifunctional Lightweight Materials and Structures (MLMS), Nanjing University of Aeronautics and Astronautics, Nanjing 210016, PR China

^d School of Mechanical Engineering, Xi'an Jiaotong University, Xi'an 710049, PR China

^e State Key Laboratory for Strength and Vibration of Mechanical Structures, Xi'an Jiaotong University, Xi'an 710049, China

ARTICLE INFO

Keywords:

Polymeric composites
Ballistic resistance
Finite element analysis
Encapsulated structures

ABSTRACT

The ballistic performance of ultra-high molecular weight polyethylene (UHMWPE) laminated plates and UHMWPE encapsulated aluminum structures were numerically characterized. Full three-dimensional continuum model for each type of target was built, and the UHMWPE was simulated using a sub-laminate approach with a composite material model. Simulation results were compared with existing experimental measurements, with good agreement achieved both on final deformation morphology and ballistic data. Underlying penetration mechanisms of laminated plate were then explored, and the effect of interface strength was quantified. The ballistic improvement of UHMWPE encapsulated aluminum structures was mainly attributed to the stretching of lateral swathing laminates. However, the benefit of encapsulation decreased as the initial impact velocity or lateral dimensions of encapsulated structure were increased. These findings are helpful for designing lightweight UHMWPE composite structures with superior ballistic resistance.

1. Introduction

Armor systems for ballistic protection are increasingly constructed with ultra-high molecular weight polyethylene (UHMWPE) fiber composites for their low density and superior mechanical properties. UHMWPE composite laminates with a $[0^\circ/90^\circ]$ cross-ply architecture have exhibited advantages in defending small caliber ballistic threats, such as fragments [1,2], projectiles [3] and spheres [4–6]. Moreover, the UHMWPE cross-ply laminates were found to be consistently more mass efficient than other common metallic and composite materials for a wide range of thickness [7].

The failure modes of UHMWPE cross-ply laminates under ballistic impact include fiber fracture, delamination, ply splitting and buckling [8–10]. Further, UHMWPE laminates fail progressively, with the depth of penetration increasing with impact velocity [11–13]. For thicker laminates, the penetration process can be divided into two stages. The first stage is accompanied by local deformation and failure caused by indirect tension [12,14] or shear plugging [13]. The second is a bul-

ging stage controlled by membrane stretching, with large out-of-plane deflection of the un-penetrated portion of the laminate, resulting in more energy absorbed than that of the first stage.

Due to the large deformation characteristics of UHMWPE cross-ply laminates, fibers at the clamping boundary are easily fractured and/or pulled out [15–17]. To avoid grip region laminate failure modes, a wrapping technique was proposed [18,19]. Two strips of Dyneema® HB26 pre-preg tape were alternatively used to wrap around an aluminum plate or an aluminum-alumina hybrid panel, and the wrapped samples were subsequently consolidated in a hot press using a die. Enhanced ballistic limit was observed compared with a target of identical areal density but without encapsulation.

Several attempts have been made to numerically simulate the ballistic response of UHMWPE cross-ply laminates. A mesoscale model was proposed by bundling fibers in strips as solid elements with orthotropic properties [20], which is nonetheless computationally expensive, thus restricting its usefulness for large scale simulations. A solid element continuum approach with a non-linear orthotropic material

* Corresponding authors at: State Key Laboratory of Mechanics and Control of Mechanical Structures, Nanjing University of Aeronautics and Astronautics, Nanjing 210016, PR China.

E-mail addresses: cyni@nuaa.edu.cn (C.-Y. Ni), tjlu@nuaa.edu.cn (T.J. Lu).

<https://doi.org/10.1016/j.compstruct.2020.112686>

Received 4 December 2019; Revised 31 May 2020; Accepted 2 July 2020

Available online 7 July 2020

0263-8223/© 2020 Elsevier Ltd. All rights reserved.

model was also developed [21], but the deformation was poorly simulated using this approach, causing significant under-prediction of the ballistic limit velocity in practical cases. To address this issue, the model was advanced using a sub-laminate discretization approach [22]: experimental data were then predicted successfully and large deflection deformation was well captured. More recently, the solid element continuum model was constructed using a similar sub-laminate approach as well as a readily available material model within LS-DYNA, and validated for Dyneema® HB26 over a range of loading conditions [23].

As for the modeling of hybrid UHMWPE/metal plates, there existed only a few attempts. Ortega et al. [24] used a multi-scale numerical constitutive model to predict the ballistic protection of external steel plates and internal UHMWPE fabrics, applicable to resin free needle-punched nonwoven dry fabrics. Liu et al. [25] simulated a ceramic composite armor containing a Ti6Al4V/UHMWPE/Ti6Al4V backing plate, in which the UHMWPE was modelled by eight node continuum shell elements. Cai et al. [26] analyzed the dynamic response of a sandwich panel with aluminum foam/UHMWPE laminate core, and the constitutive response of the laminate was simulated via a nonlinear orthotropic material model. However, thus far, the delamination failure mode and large bulge deformation of UHMWPE laminates observed experimentally had not been reproduced well by the existing models.

At present, few precise numerical studies have been conducted on UHMWPE composites having multi-material structures, especially for the encapsulated structures. Moreover, as the main purpose of existing researches on was placed upon validating the proposed numerical techniques, the physical mechanisms underlying UHMWPE composites remain to be explored. Last but not the least, the material models used by current continuum models are complicated and contain a large number of parameters, making it hard to recalibrate for other types of UHMWPE composites. Therefore, in the current study, a solid element continuum methodology with a relatively simple material model was developed. For the first time, the ballistic performance of UHMWPE encapsulated aluminum structure was numerically analyzed. For validation, the numerical simulation results were compared with experimental results of pure laminated plates [13] and encapsulated aluminum structures [18]. Finally, the penetration process, stress distribution, and mechanisms underlying the ballistic performance were systematically explored.

2. Numerical simulation model

2.1. Material

The cross-ply UHMWPE laminate employed in this study was a representative commercial grade Dyneema® HB26, which had a SK76 fiber volume fraction of 83% and a matrix of polyurethane. The 17 μm diameter SK76 fibers had a tensile strength of 3.6 GPa and an elastic modulus of 116 GPa. Bundles of fibers were coated by polyurethane to form a 67 μm thick, unidirectional ply. The HB26 pre-preg tape comprised four of these plies in the configuration of $[0^\circ/90^\circ]_2$. A laminated panel of arbitrary thickness could then be made by stacking and hot pressing the pre-preg.

Manufacturing defects in the HB26 plate had been evaluated by O'Masta et al. [27] through a combination of optical and ultrasonic imaging in conjunction with micro-X-ray tomography. Two classes of defects had been identified. One consisted of equal spaced tunnel cracks resulting from anisotropic thermal contraction of the laminates after processing, and the other consisted of void-like defects resulting from missing groups of fibers, which could be traced to the as-received prepreg tape. A porosity of 3% and 10% were calculated in low optical and high optical attenuation region, respectively, and further analysis indicated that tunnel cracks had negligible effect on compressive

strength. However, it is difficult to consider these defects in a phenomenological constitutive model, because the phenomenological model reflects only the overall performance of the material. Besides, as a widely used commercial grade, HB26 had been extensively investigated and its mechanical properties found quite stable. Therefore, for simplicity, the effects of defects were ignored in the present study.

2.2. Target model

Numerical simulations based upon the finite element method (FEM) were performed with the commercial software LS-DYNA. To simulate the layered nature of the laminates, three-dimensional (3D) sub-laminate model was employed, as shown schematically in Fig. 1. It has been demonstrated that using continuum shell elements for fiber-reinforced composite layers, which is typical in existing FE analyses, could not provide reliable predictions for multi-material structures, due to the necessity of realistic modeling of the interface between different components and composite layers [28]. Moreover, the stresses in the thickness direction were believed to be important for the laminate subjected to impact, so solid elements were selected in the present study instead of shell elements.

The sub-laminate model, first proposed by Nguyen et al. [22] and then adopted by Hazzard et al. [23], had been shown to accurately capture the out-of-plane deformation of UHMWPE composites. Generally, it is difficult to simulate the delamination and large back-face deflection of UHMWPE laminates using continuum models. In the present study, the bulk laminate was modeled as a combination of several sub-laminates which were joined together, while each sub-laminate was modeled as a homogenization of several cross-plys. Consequently, the countless interfaces in a typical cross-ply laminate were reduced to several interfaces in the continuum model such that numerical simulation of the delamination failure mode could be achieved by defining the failure between sub-laminates. The interface thickness between two adjacent sub-laminates was taken as zero, and nodes in one were detached from nodes in the other. The strength of the interface was defined by cohesive tied contact, as described in the following section.

Two types of target model were constructed, as shown in Fig. 2. The first type, presented in Fig. 2(a), was built as the same cross-ply laminated plate used in the experiments of Nguyen et al. [13], with in-plane dimensions of 300 mm \times 300 mm and a thickness of 10 mm. The projectile adopted was fragment-simulating projectile (FSP) made of 4340H steel, with a diameter of 20 mm and a mass of 54 g [29].

A mesh refinement study was performed to determine the suitable element size within the penetration zone. The central element size was varied from 0.5 mm to 2 mm, with an aspect ratio of unity. Besides, the mesh of the target and projectile was matched to avoid a stiffness mismatch. An initial velocity of 648 m/s was applied to the projectile, and the numerical results of residual velocities were compared in Table 1 with that measured experimentally (583 m/s). The predicted residual velocity was found to increase with decreasing mesh density. Further, numerical convergence and high accuracy could be approximately reached for cases having element sizes smaller than 0.83 mm. Typical runtimes for a 10 mm target with a 0.66 mm central mesh size were less than 1 h, only a quarter of the runtime taken by the numerical model reported in Hazzard et al. [23]. Following the mesh sensitivity studies, a 0.66 mm central mesh with a bias to 2.8 mm at the outer edge was selected, which was a compromise between the accuracy of numerical simulation results and computational cost. The 0.66 mm sub-laminate corresponded to a HB26 laminated plate with configuration $[0^\circ/90^\circ]_5$. The element size of the FSP was 0.6 mm. In total, the projectile was meshed with 32,700 elements, and the 10 mm thick laminated plate was meshed with 937,500 elements. To better understand the post-impacted morphology of thicker laminates, 36 mm and 50 mm thick laminates were also simulated.

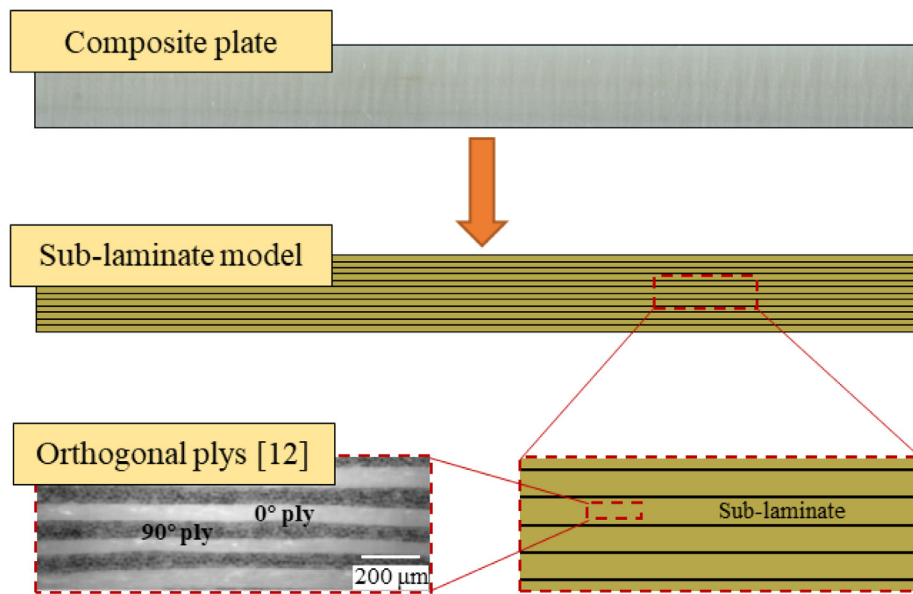


Fig. 1. Schematic of sub-laminate model for cross-ply UHMWPE laminated plate.

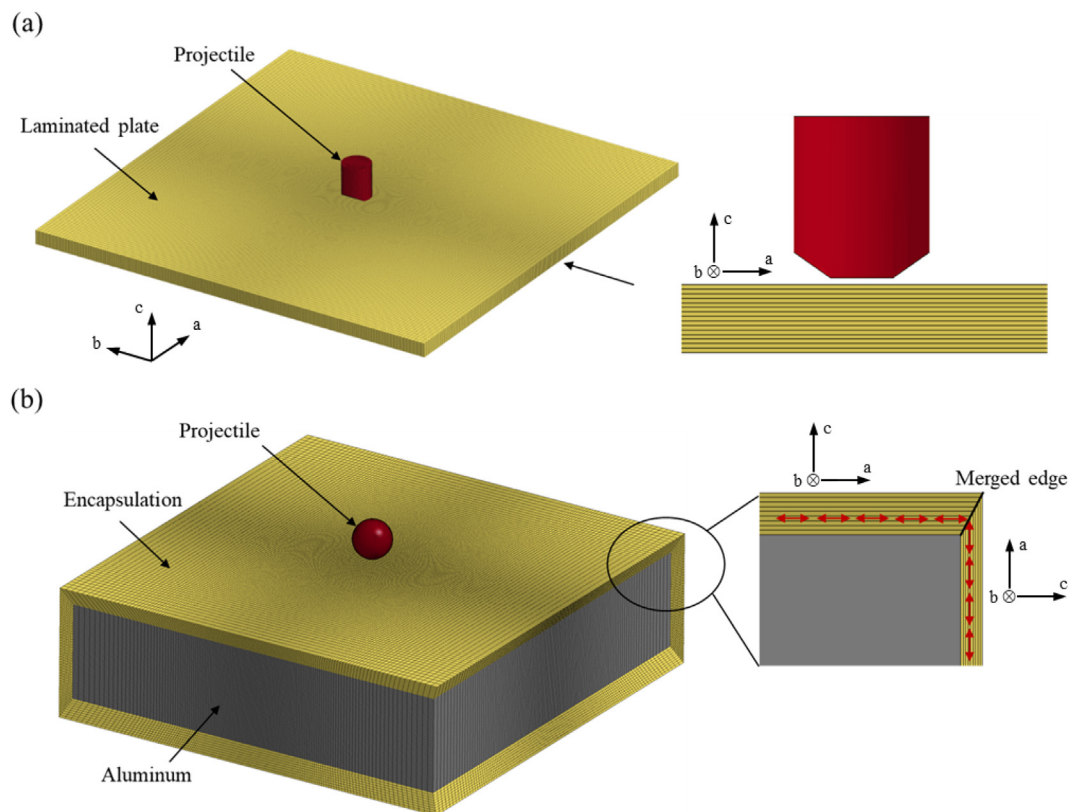


Fig. 2. Numerical models for (a) laminated plate and (b) encapsulated aluminum structure. The out-of-plane direction was designated as the 'c' direction, and the fiber directions were the 'a' and 'b' directions. The symbol '⊗' represented the inward direction.

The second type of target, presented in Fig. 2(b), was the Dyneema® encapsulated aluminum structure proposed by O'Masta et al. [18]. In their experiments, two strips of HB26 pre-preg tapes were used to wrap alternatively the 132 mm × 136 mm × 831.6 mm thick 6061-T6 aluminum (Al) plate, and then the wrapped sample was consolidated in a hot press using a die. The final fully encased target had 5.9 mm thick laminates on both the front and rear faces of the

Al plate, and 2.95 mm thick laminates on the four lateral faces. The hardened 52,100 chrome steel sphere projectile with 12.7 mm in diameter and 8.4 g in weight was used to impact the center of the target. In the present FEM simulation model, the encapsulation was divided into three parts including the front face, the rear face and the lateral faces. The element thickness selected for the 5.9 mm UHMWPE encapsulation was 0.65 mm. The mesh size of the impact

Table 1
Mesh sensitivity for 10 mm UHMWPE laminated plate impacted at 648 m/s.

Central element size (mm)	Number of sub-laminates	Residual velocity (m/s)	Difference from tests (%)	Computational time (s)
2.00	5	533	8.6	108
1.25	8	566	2.9	582
0.83	12	576	1.2	1253
0.71	14	579	0.7	2212
0.66	15	581	0.3	2601
0.50	20	586	0.5	4693

region was 0.5 mm both for encapsulation and aluminum, which was comparable to the element size of the sphere projectile (minimum size 0.3 mm). It could be inferred from Table 1 that the mesh strategy adopted for the UHMWPE encapsulation could also provide enough accuracy for FE simulation. In total, the projectile, the Al plate and the Dyneema® encapsulation were separately meshed with 22880, 1,154,200 and 639,100 elements.

In order to simulate the interaction between laminates on different faces, nodes on intersecting edges were merged together. As the fiber direction was different on each part, locally orthotropic material axes were independently defined, as shown in Fig. 2(b), to ensure the fibers were aligned along the in-plane direction and remained continuous at the intersect edge. Contact between the Al plate and the encapsulation was modeled as Automatic-Surface-To-Surface, while contacts between the projectile and sub-structures of the target plate were achieved with the Eroding-Surface-To-Surface. A soft constraint type 2, pinball based segment contact, was added in the eroding contact between the projectile and target, which was more effective for contact between materials having dissimilar stiffness or dissimilar mesh densities. To counter the non-physical modes of deformation, an hour-glass control methodology of type 5, Flanagan-Belytschko stiffness form with exact volume integration for solid elements, was employed. Moreover, the invariant node numbering for solid elements was on, which was recommended when solid elements of anisotropic material undergo significant deformation.

2.3. Material model

A composite material model with failure criteria for solid element was selected to model the behavior of homogenized sub-laminates, which was the material type #59 within LS-DYNA. The Dyneema® HB26 was assumed to be orthotropic, with a linear elastic relation between stress and strain described as:

$$\begin{Bmatrix} \varepsilon_a \\ \varepsilon_b \\ \varepsilon_c \\ \gamma_{bc} \\ \gamma_{ca} \\ \gamma_{ab} \end{Bmatrix} = \begin{bmatrix} \frac{1}{E_a} & -\frac{\nu_{ba}}{E_b} & -\frac{\nu_{ca}}{E_c} & 0 & 0 & 0 \\ -\frac{\nu_{ab}}{E_a} & \frac{1}{E_b} & -\frac{\nu_{cb}}{E_c} & 0 & 0 & 0 \\ -\frac{\nu_{ac}}{E_a} & -\frac{\nu_{bc}}{E_b} & \frac{1}{E_c} & 0 & 0 & 0 \\ 0 & 0 & 0 & \frac{1}{G_{cb}} & 0 & 0 \\ 0 & 0 & 0 & 0 & \frac{1}{G_{ca}} & 0 \\ 0 & 0 & 0 & 0 & 0 & \frac{1}{G_{ab}} \end{bmatrix} \begin{Bmatrix} \sigma_a \\ \sigma_b \\ \sigma_c \\ \tau_{bc} \\ \tau_{ca} \\ \tau_{ab} \end{Bmatrix} \quad (1)$$

where E , G and ν were the elastic modulus, shear modulus and Poisson ratio of the composite laminate, and the subscripts a , b , and c denoted local element axes. In this work, the 0° and 90° directions of the laminate were designated as the a and b directions, respectively, and c represented the through-thickness direction. Due to the cross-ply layout, material properties along 0° and 90° directions could be taken as equal. Table 2 listed the orthotropic elastic parameters of the laminate.

Failure modes and the corresponding criteria adopted by the composite material model were summarized in Table 3. Eight failure modes and nine strengths were implemented in the material model, including three shear strengths (S_{ab} , S_{ac} , S_{bc}), three compressive strengths (C_a , C_b , C_c) and three tensile strengths (T_a , T_b , T_c). However, only the in-plane tensile strengths and the out-of-plane compressive

Table 2
Material parameters for Dyneema® HB26 [10,21,23,35].

Parameter	Value	Parameter	Value
<i>Elastic property</i>		<i>Strength and failure</i>	
Young's modulus, E_a (GPa)	34.257	Tensile strength, T_a (GPa)	1.25
Young's modulus, E_b (GPa)	34.257	Tensile strength, T_b (GPa)	1.25
Young's modulus, E_c (GPa)	3.26	Compressive strength, C_c (GPa)	1.9
Poisson's ratio, ν_{ba}	0		
Poisson's ratio, ν_{ca}	0.013		
Poisson's ratio, ν_{cb}	0.013		
Shear modulus, G_{ab} (GPa)	0.1738	<i>Sub-laminate interface</i>	
Shear modulus, G_{ca} (GPa)	0.5478	Normal strength, I_n (MPa)	1.2
Shear modulus, G_{cb} (GPa)	0.5478	Shear strength, I_s (MPa)	2.6

Table 3
Failure criterion of composite material model.

Failure mode	Criterion
In-plane tensile failure	$\left(\frac{\sigma_a}{T_a}\right)^2 + \left(\frac{\tau_{ab}}{S_{ab}}\right)^2 + \left(\frac{\tau_{ac}}{S_{ac}}\right)^2 \geq 1$ (1)
	$\left(\frac{\sigma_b}{T_b}\right)^2 + \left(\frac{\tau_{ab}}{S_{ab}}\right)^2 + \left(\frac{\tau_{bc}}{S_{bc}}\right)^2 \geq 1$ (2)
Through-thickness tensile failure	$\left(\frac{\sigma_c}{T_c}\right)^2 + \left(\frac{\tau_{ac}}{S_{ac}}\right)^2 + \left(\frac{\tau_{bc}}{S_{bc}}\right)^2 \geq 1$ (3)
Through-thickness shear failure	$\left(\frac{\sigma_a}{T_a}\right)^2 + \left(\frac{\tau_{bc}}{S_{bc}}\right)^2 \geq 1$ (4)
	$\left(\frac{\sigma_b}{T_b}\right)^2 + \left(\frac{\tau_{ca}}{S_{ca}}\right)^2 \geq 1$ (5)
Longitudinal compressive failure	$\left(\frac{\sigma_c}{C_c}\right)^2 \geq 1$ (6)
Through-thickness and transverse compressive failure	$\left(\frac{\sigma_b}{S_{ab}+S_{bc}}\right)^2 + \left[\left(\frac{C_b}{S_{ab}+S_{bc}}\right)^2 - 1\right] \frac{\sigma_b}{ C_b } + \left(\frac{\tau_{ab}}{S_{ab}}\right)^2 + \left(\frac{\tau_{bc}}{S_{bc}}\right)^2 \geq 1$ (7)
	$\left(\frac{\sigma_c}{S_{ac}+S_{bc}}\right)^2 + \left[\left(\frac{C_c}{S_{ac}+S_{bc}}\right)^2 - 1\right] \frac{\sigma_c}{ C_c } + \left(\frac{\tau_{ac}}{S_{ac}}\right)^2 + \left(\frac{\tau_{bc}}{S_{bc}}\right)^2 \geq 1$ (8)

strength were used in the present study, with the remaining strengths set to infinite values. The in-plane tensile strengths were defined to simulate fiber tensile fracture, with their values approximated from single ply tests and digital image correlation of laminate tensile tests [23]. Out-of-plane compressive failure was found to be induced by the indirect tension mechanism [14], in which the fiber tension stress was generated by compression-induced anisotropic plastic expansion of the alternating $0^\circ/90^\circ$ plies. The out-of-plane compressive strength was estimated to be 1.9 GPa from quasi-static indentation tests [10]. Through-thickness and in-plane shear strengths were not considered due to the large strain at failure [21]. Further, in-plane compressive failure of Dyneema® laminates dictated by micro-buckling and kink-band formation was ignored, for it had little influence on penetration resistance [30].

Additional scaling factors were applied to various components of stress, and degradation was performed over a small period of time. Once a failure mode was triggered, it took 100 time steps for the corresponding scaling factors to change from a starting value of 1.0 to a final value of zero, thereby reducing the stress components to zero. Elimination of the failed elements was achieved by defining a maximum tensile strain of 0.4 and a compressive volumetric strain of 0.8.

Thermal softening was not considered. As the matrix volume fraction of Dyneema® HB26 is very low, and it has been confirmed that strain rate effect is not significant for UHMWPE fibers [31,32], strain rate dependency was not considered in the current numerical model.

Interfaces between the sub-laminates were implemented by tie-break contacts, defined as:

$$\left(\frac{\sigma_n}{I_n}\right)^2 + \left(\frac{\sigma_s}{I_s}\right)^2 \geq 1 \quad (2)$$

where σ_n and σ_s were the normal and shear stresses, and I_n and I_s were the normal and shear failure strengths. Before interface failure occurred, nodes in contact were stick and tangential motion was inhibited. After the interface had failed, this contact option would behave as a surface-to-surface contact and no interface tension was possible. As a result, interlaminar delamination of the laminate could be numerically achieved.

The Johnson-Cook constitutive and failure models were employed for both the 4340H steel FSP [22] and the 6061-T6 aluminum plate [33], with the corresponding material parameters as listed in Table 4. Besides, the hardened 52,100 chrome steel sphere projectile used in the encased target was set as rigid material because its high compressive yield and failure strength [34] compared to the targets.

3. Validation

3.1. Determination of boundary conditions

To validate the present numerical simulations, existing experimental results of Nguyen et al. [13] and O'Masta et al. [18] were used. During the tests, the pure laminated plate was clamped to a steel frame, while a fixture was employed to hold the encapsulated target in posi-

Table 4
Material parameters for 4340H steel [22] and 6061-T6 Al [33].

Material/constants	Steel 4340	Al 6061-T6
Density, ρ (kg/m ³)	7800	2700
Shear modulus, G (GPa)	77.0	27.6
Bulk modulus, K_1 (GPa)	150	77
Static yield strength, A (GPa)	1.030	0.324
Strain hardening constant, B (GPa)	0.477	0.114
Strain hardening exponent, n	0.18	0.42
Strain rate constant, C	0.012	0.002
Thermal softening exponent, m	1.0	1.34
Reference strain rate, $\dot{\epsilon}_0$ (s ⁻¹)	1.0	1.0
Melting temperature, t_m (K)	1793	893
Specific heat, C_r (J/kg · K)	477	885
Damage constant, d_1	3.0	-0.77
Damage constant, d_2	0	1.45
Damage constant, d_3	0	-0.47
Damage constant, d_4	0	0
Damage constant, d_5	0	1.06

tion. To explore the influences of boundary conditions, FE simulations were carried out on the UHMWPE laminated plate, and four different boundary conditions were analyzed: Clamp A, Clamp B, free boundary and fixed boundary, as shown in Fig. 3. Clamping conditions A and B were used to mimic the boundary conditions applied in the UHMWPE laminated plate [13] and the encapsulated target [18], respectively. With the initial impact velocity of 443 m/s fixed for all the models, the calculated residual projectile velocities (V_R) were compared. The results showed similar deformation and failure modes in the target plates with different boundary conditions: Clamp A, Clamp B and free. As a result, the residual velocities of the three cases were close to each other. However, when the boundary was fully clamped, bulge deformation was significantly changed, as displayed in Fig. 3. In this case, pull in (slippage) at the boundary was prohibited, resulting in increased membrane tensile stressing and boundary failure. Further, the corresponding residual velocity of 250 m/s was larger than the other three cases: 208 m/s for Clamp A boundary, 217 m/s for Clamp B boundary and 219 m/s for free boundary.

Indeed, in the experimental of Nguyen et al. [13] and O'Masta et al. [18], little constraints had been applied in the in-plane direction of the target plate. Due to the low coefficient of friction of Dyneema®, high speed video of ballistic tests typically showed clamp slippage upon impact. In the current study, as the plate was large enough in comparison with the projectile, the clamping condition was approximated as free boundary, i.e., no boundary conditions were imposed on the targets in the present numerical models.

3.2. Validation

Fig. 4 compared the present numerical results of the 10 mm laminated plate with existing experimental data. Excellent agreement was achieved for both the residual velocity (V_R) and ballistic limit velocity (V_{BL}). The maximum error between numerical and experimental residual velocity values was 13.2% (at an impact velocity of 443 m/s), and the deviations were less than 40 m/s in absolute value for all predictions. The relationship between the impact velocity (V_i) and V_R was also fitted to the Lambert-Jonas equation shown in Fig. 4(a), as:

$$V_R = a(V_i^p - V_{BL}^p)^{1/p} \quad (3)$$

where a and p were determined from a least squares fit of numerical results and V_{BL} was estimated by $V_R = 0$. Further, as shown in Fig. 4(b), the out of plane deformation feature of the laminated plate was also well replicated in the current numerical model. The discrepancy between the numerical and experimental results slightly increased after 200 μ s, leading to a maximum error of 7.5%, possibly because the simplification of interface properties and the omission of thermal softening in the model.

In Fig. 5, the experimentally observed deformation and failure morphology of a 36 mm thick laminate were compared with those numerically simulated. The two penetration stages were captured well by the

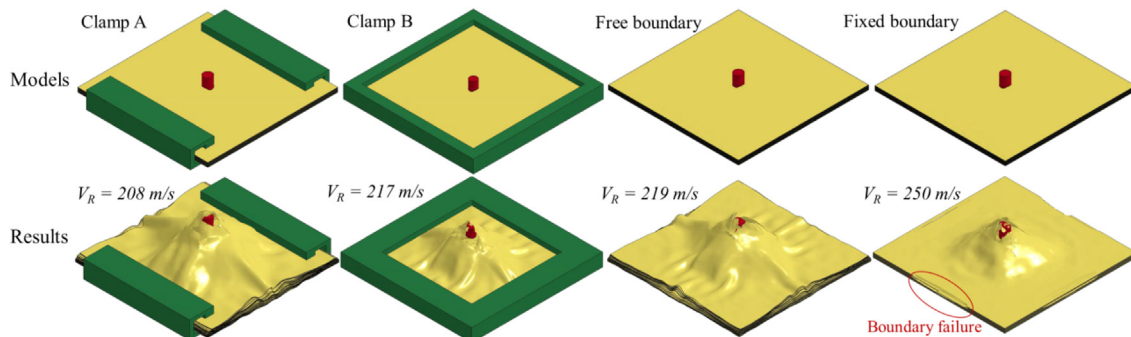


Fig. 3. Numerical models and simulated results for target plates with four different types of boundary condition.

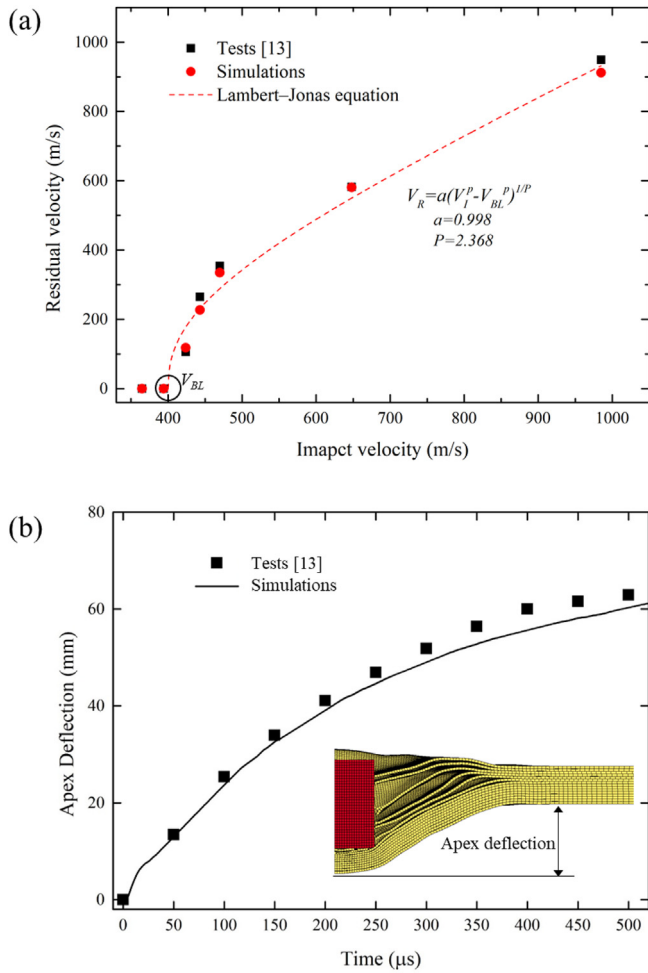


Fig. 4. Comparison between numerical prediction and experimental measurement of (a) residual velocity and (b) apex deflection of 10 mm Dyneema® laminate impacted by 20 mm FSP.

model: the first stage was characterized by local deformation and failure immediately under the projectile, and the second stage was characterized by large bulge deformation. In the transition zone from the first to the second stage, large amounts of delamination were visible, as shown in Fig. 5(b). Further, laminate folding and pull-in effect at the boundary were also simulated successfully.

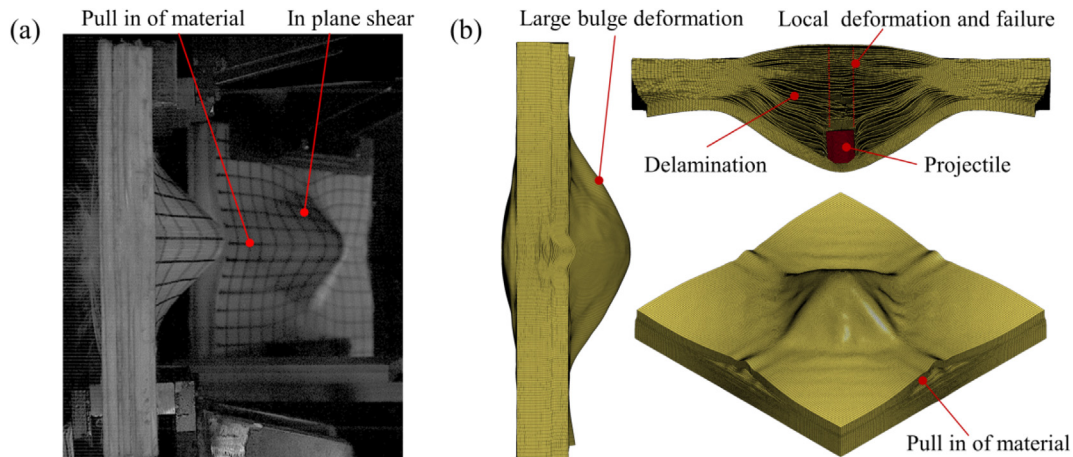


Fig. 5. (a) A high speed image of 36 mm thick laminate at 200 μ s after impact by a 20 mm FSP [13], compared to (b) numerical simulation results of deformation and failure response.

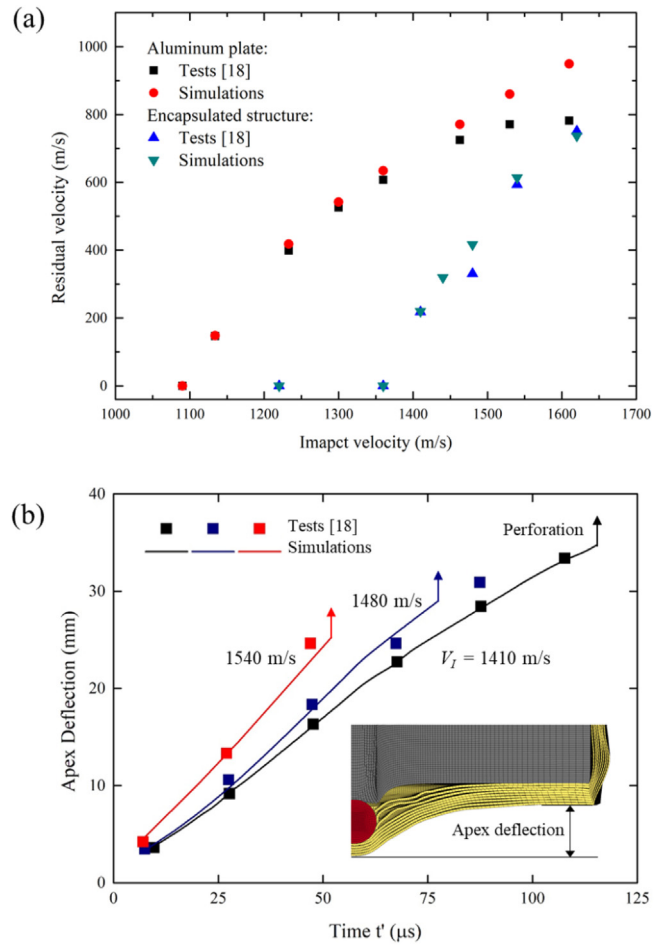


Fig. 6. (a) Residual velocity of bare aluminum plate and Dyneema® encapsulated aluminum structure; (b) Apex deflection of Dyneema® rear face at different impact velocities, and time $t' = 0$ corresponded to the instant that the deformation of the rear Dyneema® face initiated.

Numerical results for both bare and encapsulated target plates were presented in Fig. 6. The numerical residual velocities for bare Al plates agreed well with existing test data when the impact velocity was less than 1300 m/s, but deviated from the test data as the impact velocity was increased, as shown in Fig. 6(a). The numerical over-prediction was attributed to projectile fragmentation when the impact velocity

exceeded 1300 m/s, as observed in the experiment [18]. At lower impact velocities, projectile fragmentation did not occur so the projectile could be treated as rigid consistently in the numerical model. In contrast, because placing the low-impedance Dyneema® on the front face could prevent the fracture of projectile, the projectile would remain intact for the encapsulated structure. Therefore, as shown in Fig. 6(b), for encapsulated structure, the numerically calculated residual velocity as well as the apex deflection agreed fairly well with experimental measurements.

The results presented in Figs. 4–6 demonstrated the feasibility and validity of the numerical models developed in the present study.

4. Discussion

4.1. UHMWPE laminated plates

4.1.1. Penetration mechanisms

Fig. 7(a) plotted the numerically computed projectile contact force as a function of time for 10 mm laminated plates impacted at three different velocities and for a 50 mm laminated plate impacted at 1100 m/s. It could be drawn from the curves that the contact force increased sharply within the initial few microseconds after the impact was initiated, as its peak value increased with the impact velocity. Afterwards, the contact force would drop sharply at around 10 μ s for the 10 mm target while at around 37 μ s for the 50 mm target. To explore the underlying mechanism, contours of compressive stress in the thickness

direction of the 10 mm target were plotted in Fig. 7(b). Once the impact was initiated, a compressive shockwave was emanated from the impact surface, reaching the rear face at $\sim 5 \mu$ s. Subsequently, the compressive stress wave would reflect as a tensile wave from the free rear face and arrived at the penetrating projectile front end within 10 μ s, thus reducing the contact force. Detailed examination of the numerical results for the 50 mm target also revealed that the drop of contact force was related to the tensile relief wave. The speed of this compressive shockwave was calculated as ~ 2200 m/s, which was close to that (2500 m/s) deduced from measurements [9].

The contact force is an important parameter in the failure analysis of composite laminates. For example, the produced compressive pressure was related to local deformation and failure at the front surface (Fig. 5). It is noted from Fig. 7(a) that, for thicker laminates, the duration of this huge pressure was longer. As a consequence, a larger portion of the laminate would fail in a locally progressive manner, while this failure mode was almost invisible in thinner laminates. After the drop of contact force, the pressure gradually decreased and eventually became insufficient to cause local failure. This would then activate the membrane stretching response of the remaining intact portion of the laminate, leading to large bulge deformation especially for impact velocities below the ballistic limit.

Fig. 8 displayed the simulated deformation process of 10 mm laminates at selected times, in which the contours of maximum principal stress were also included. The elements in 'blue' indicated that the tensile stress had already reached or were about to reach the tensile strength of 1250 MPa and would be deleted in the next few time steps. For a laminate impacted near ballistic limit (394 m/s), a zero out-of-plane deformation of the rear face was observed until the compressive shock wave had reached it at $\sim 5 \mu$ s. As the projectile impacted the target, a longitudinal tensile wave was formed, emanating from the impact location and travelling along the fiber direction. This longitudinal tensile wave would cause the pull-in effect from the edges when it reached the lateral free boundary. Subsequently, the wave would be reflected and return to the impact region at $\sim 52 \mu$ s, leading to the release of tensile stress immediately under the impactor, which was taken as an unloading mechanism to the penetration process after $\sim 52 \mu$ s. Therefore, the membrane stretching stress would remain relatively small afterwards, with the bulge grown larger and the velocity of projectile decreased.

Perforation of the laminated plate was controlled by maximum tensile stress at the rear face, which could be observed at $\sim 9 \mu$ s, caused by local bending of sub-laminate during the initial stage of bulge formation. For the laminate impacted at 394 m/s, its tensile strength had not been reached at the rear face, so the projectile was fully stopped at the membrane stretching stage. When the impact velocity was increased to 470 m/s, in some elements on the rear face the tensile strength would be reached. During subsequent penetration, the unpenetrated remainder sub-laminates with premature failure would provide less resistance and be fully perforated at 120 μ s, as shown in Fig. 7(a). As the impact velocity was increased to 648 m/s, tensile failure of sub-laminate immediately under the projectile was observed at 2 μ s, and a larger portion of the elements failed at the rear face at $\sim 9 \mu$ s. Therefore, the mechanism of membrane stretching could not be activated, thus a shorter time would be taken to perforate the laminate.

4.1.2. Influence of interface strength

Additional FEM simulations were carried out to explore how interface strength affected the ballistic response of Dyneema® laminated plates. The results were presented in Fig. 9, with the interface normal strength I_n and shear strength I_s (described in Section 2.3 and listed in Table 2) magnified up to 1000 times. The ballistic performance of the laminate was seen to decrease with increasing interface strength. As the normal strength was 120 MPa, the residual projectile velocity was dramatically increased and then became flat with the further increase of interface strength. Failure modes for laminates with differ-

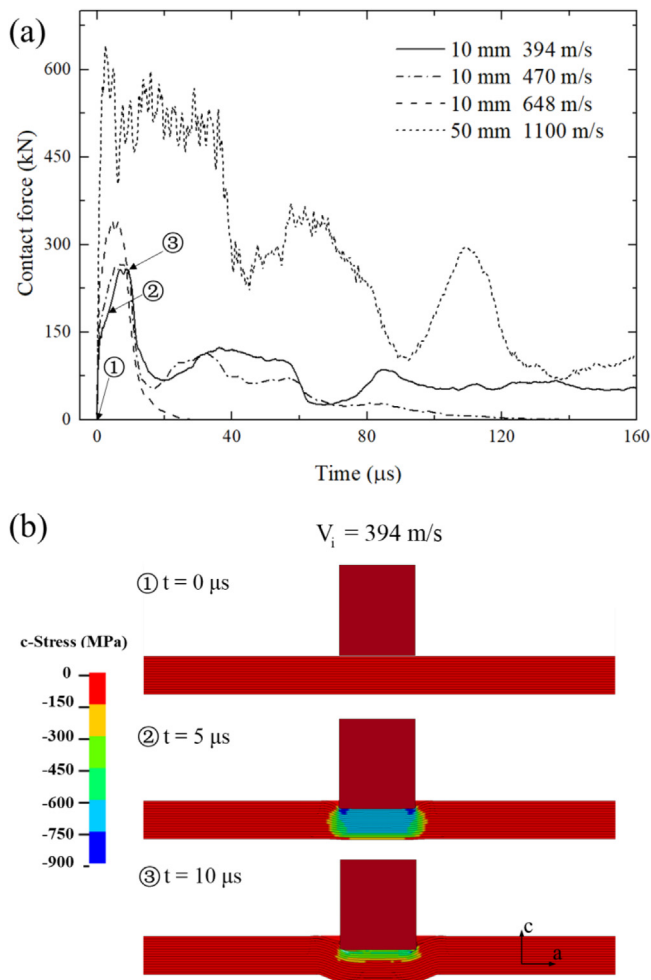


Fig. 7. (a) Contact force between FSP and laminated plate, and (b) contours of compressive stress in thickness direction.

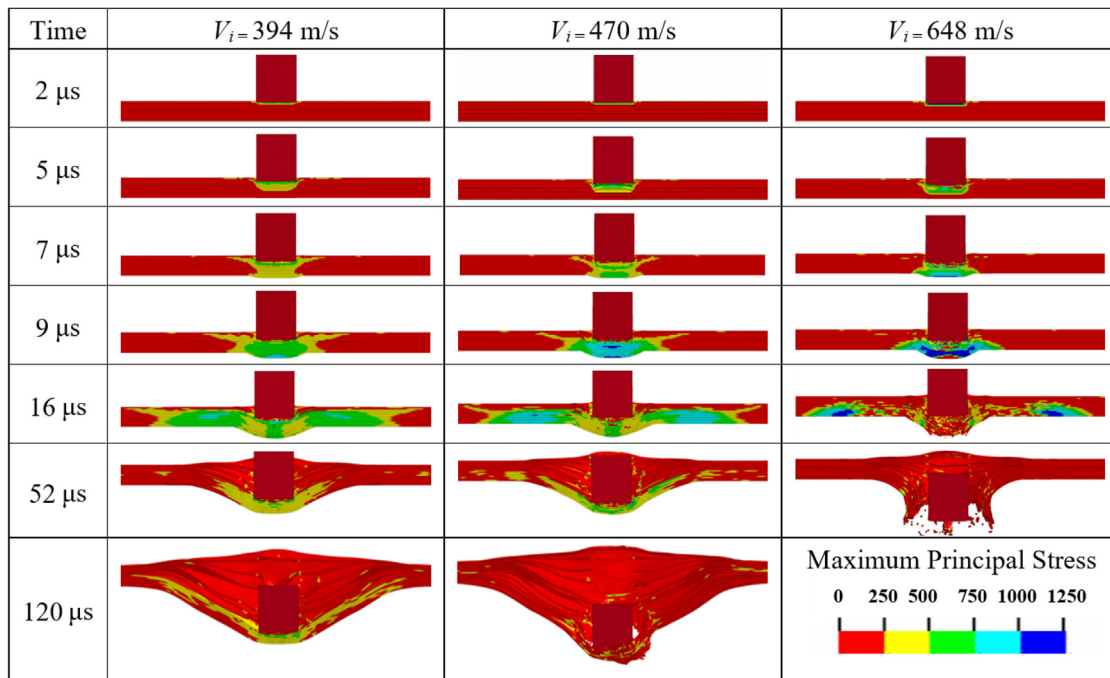


Fig. 8. Numerically simulated evolution of maximum principal stress in 10 mm laminated plate subjected to projectile impact at selected impact velocities.

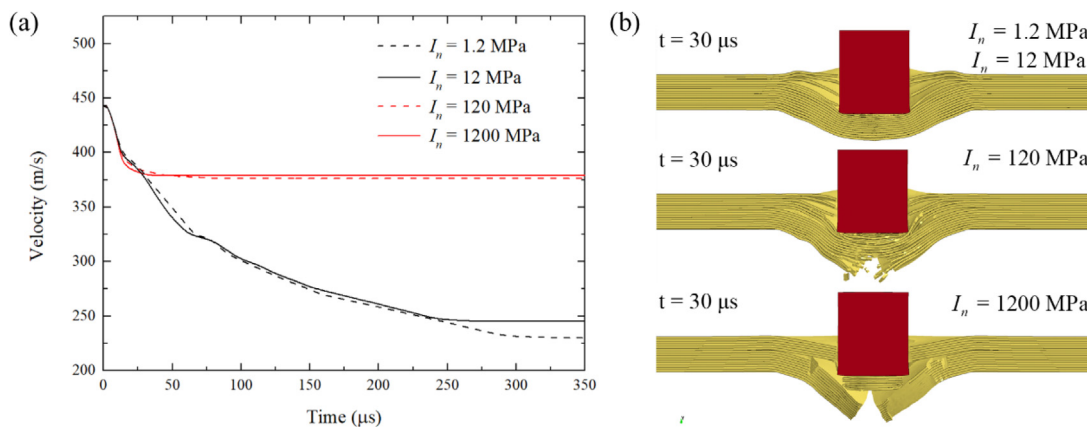


Fig. 9. (a) Velocity histories of impact projectile and (b) failure modes for laminates with different interface strengths at an impact velocity of 443 m/s.

ent interface strengths were also different, as illustrated in Fig. 9(b). For the laminate with a normal strength of 120 MPa, premature tensile failure of the rear sub-laminates was observed. When the interface strength was magnified 1000 times, a plug was sheared from the front half and the rest exhibited a petal-type failure, leaving a diamond-shaped damage after perforation: such failure phenomenon was similar to existing experimental observations of stiff carbon fiber laminates [36].

Recently, Liu et al. [37] confirmed in their mesoscale model that tensile stress in a debonded cross-ply laminate was much lower than that in cross-ply laminate with perfect bonding. This could be the mechanism underlying the effect of interface strength identified in the present study. For a laminated plate with relatively low interface strength, bending stresses across the section of the plate cannot be supported, as stress gradient arising from bending will be relieved via delamination. Consequently, a laminate with stronger interface will suffer larger bending stressing, causing premature failure of its rear face. In fact, the stress-based failure criterion employed in the current model underestimated the effect of real interface in laminates [38],

because the additional energy in cracks propagating across the interface was not described and fiber-bridging effects were neglected. However, the preliminary numerical analysis presented here were still meaningful for the design of high performance laminated plates.

4.2. UHMWPE encapsulated aluminum structures

4.2.1. Penetration process

As shown in Fig. 10, the penetration of a sphere projectile with velocity 1360 m/s into a fully encapsulated target could be described as below: at the first ten microseconds, the Dyneema® laminate on the front face would be completely perforated without significant deflection. The Al plate would then fail in the mode of ductile hole enlargement, leaving a crater diameter equal to the diameter of projectile. After the thick Al plate was perforated at around 56 μ s, the projectile would contact directly with the rear Dyneema® face. Then it would take a longer time to stop the projectile, and the apex deflection of the rear face continued to increase until 300 μ s after the impact. Meanwhile, the very large deflection of the rear face was accompanied by

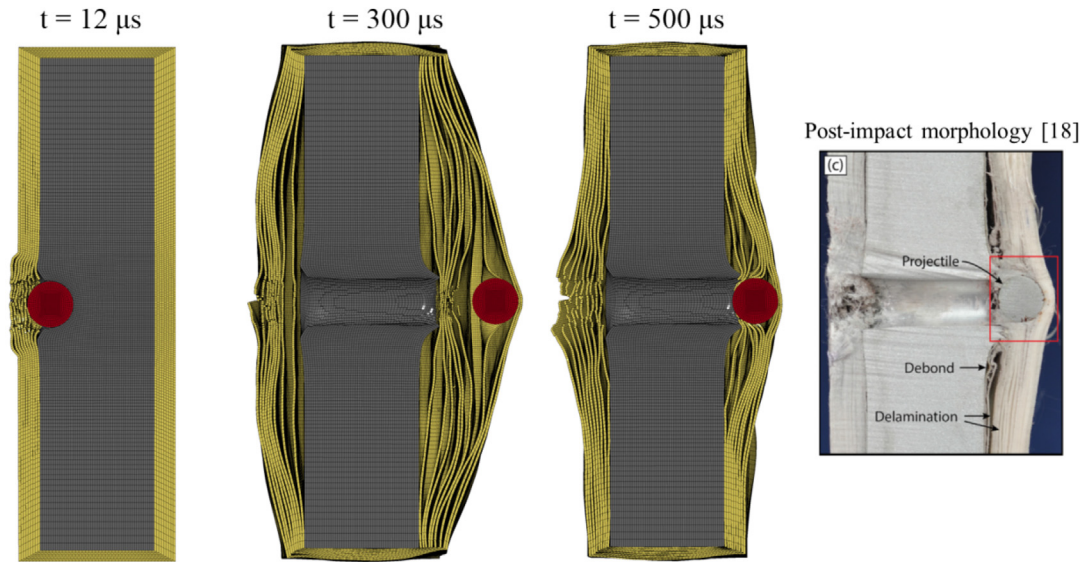


Fig. 10. Simulated penetration responses of Dyneema® encapsulated aluminum structure at impact velocity of 1360 m/s. A cross-sectional photograph taken after ballistic test [18] was also presented.

delamination of the sub-laminates and pull-in of Dyneema® from the sides. Eventually, both the projectile and the rear laminate rebounded slowly, causing a much smaller deflection to be detected in the test results [18].

Consider next the failure mechanisms of both the front and rear laminates. The laminate on the front face was back supported by Al plate, thus could not undergo significant deflection. When subjected to impact, large compressive stress generated beneath the projectile would cause the front laminate to fail in a compressive manner, as depicted in Fig. 11(a). As for the laminate on the rear face of the encapsulated structure, the compressive stress would be released by tensile wave reflected from the free face, which was thus not enough to trigger compressive failure. In this case, as shown in Fig. 11(b), tensile failure was observed in the sub-laminate making direct contact with the projectile, so that the rear laminate would fail in a progressive manner. The contact region of this sub-laminate was forced to deform in accordance with the curvature of the spherical projectile, which could be used to rationalize the tensile failure. In contrast, for a laminated plate impacted by the FSP, failure first occurred within the region beneath the sharp edges of the FSP as a result of stress concentration. This numerical conclusion had also been observed in experiment. Tan et al. [17] investigated the response of UHMWPE laminates to ballistic impacts by projectiles having various geometries,

and found that hemispherical projectiles perforated the laminates by stretching the filaments to failure whereas flat ended projectiles tended to shear the filaments. However, conical and ogival projectiles perforated the specimens mainly by pushing aside the fibers rather than breaking them, resulting in a smaller ballistic limit [39]. It should be noted that, in the present continuum model, the mechanism of fibers being pushed aside laterally had not been considered, so numerical simulation of the penetration process of sharp-nosed projectiles into UHMWPE composites remains a challenge for future studies.

4.2.2. Encapsulating effects

Fig. 12(a) presented the energy absorption capability of each component at different initial impact velocities, in terms of specific energy absorption (SEA, the ratio of internal energy to mass). As the impact velocity was increased, the SEA of the encapsulated Al plate remained relatively low while that of the front laminate increased slightly. In contrast, the energy absorption capability of the rear and lateral laminates would increase first as the impact velocity was increased, peaking at the ballistic limit, and then decreased. At impact velocities near the ballistic limit, the lateral laminates and rear laminate possessed much larger SEA values than the other two sub-structures, suggesting that membrane stretching was superior in energy absorption compared to local fracture of the front laminate. It was also worth noting that the

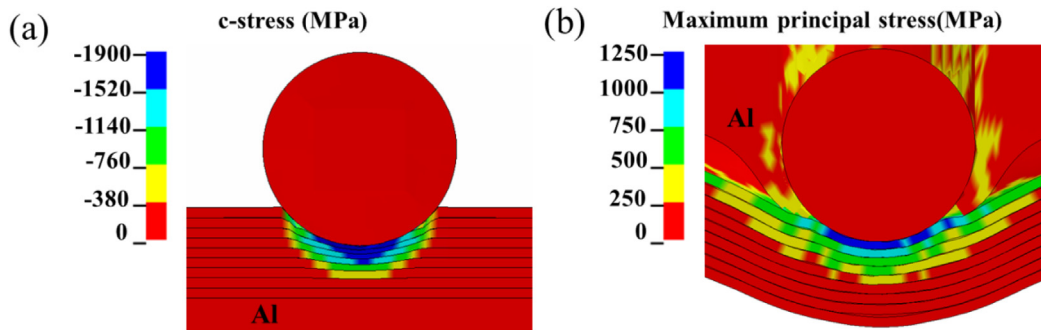


Fig. 11. UHMWPE encapsulated aluminum structure: (a) compressive stress contour of front laminate in thickness direction and (b) maximum principal stress contour of rear laminate.

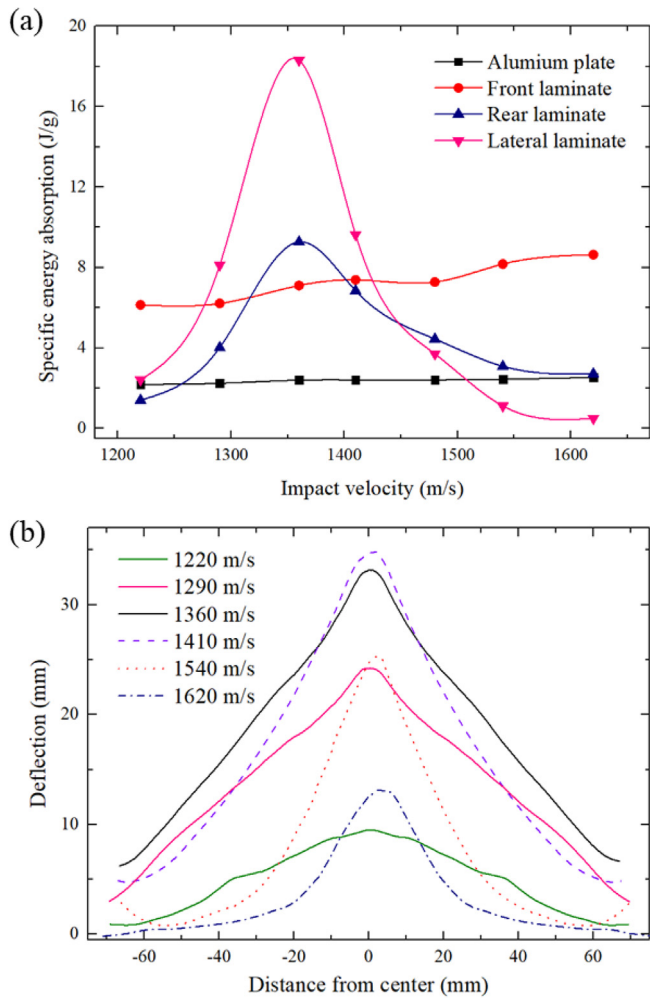


Fig. 12. (a) Specific energy absorption (SEA) of each sub-component in encapsulated structure and (b) deformation profile of rear laminate at selected impact velocities.

lateral laminates had a peak SEA value almost twice that of the rear laminate, demonstrating that the stretching of lateral laminates was the major mechanism underlying the enhanced ballistic performance of encapsulated structures.

Fig. 12(b) displayed the out-of-plane deflection profile of the rear laminate when the projectile velocity became zero or just before the perforation occurred. At the impact velocity of 1220 m/s, the projectile could just penetrate through the Al plate and be intercepted by the rear laminate without failure, resulting in a small deflection of the rear laminate (i.e., minimal membrane stretching) and thereby a low SEA. Before the ballistic limit, the deformation became larger with the increase of impact velocity. When the impact velocity exceeded the ballistic limit, the maximum deflection that the rear laminate could reach decreased, and the deflection region became more localized. Meanwhile, pull-in effects and stretching from lateral laminates gradually disappeared, which was thought to be responsible for the decrease of SEA at higher impact velocities.

To better understand the encapsulating effect, three types of composite target were simulated and compared: Dyneema® encapsulated aluminum target, layered target A with Dyneema® laminates on the front and rear faces without lateral boundary constraint, and layered target B with fixed lateral boundary condition.

Fig. 13 plotted the computed projectile velocity as a function of time for the three targets at a fixed initial impact velocity of 1360 m/s. The results demonstrated the superior ballistic performance of the encapsulated target. The encapsulated target could stop the projectile, the layered target B was perforated, while quite a few sub-laminates of layered target A delaminated fully and were carried along with the projectile, as shown in the insert of Fig. 13. Although target A was not perforated, these sub-laminates flew together with the projectile at 130 m/s, so the ballistic limit velocity of target A was considered to be smaller than 1360 m/s. As could be seen from Fig. 13, discrepancy among the three projectile velocities started to appear around 75 μs and gradually increase thereafter, implying that the encapsulating effects were in force as the projectile was penetrating the rear laminate.

Fig. 14 compared the deformation and failure of the rear laminate for the three targets evaluated in Fig. 13. First, for the encapsulated target, the rear laminate was pulled in towards the penetration region, causing the lateral laminates to stretch. This in-plane stretching of the lateral laminates could take more advantage of the high tensile strength of UHMWPE fibers, thereby enabling the lateral laminates to acquire the highest SEA. Secondly, for the layered target A, due to the loss of lateral boundary constraint, the pull-in effect was more obvious. However, several sub-laminates would eventually separate from the target structure and fly together with the projectile, thereby failing to fully exert resistance to the projectile. Thirdly, when the fixed boundary condition was in force, the longitudinal tensile stress could not be released. In other words, the sub-laminates

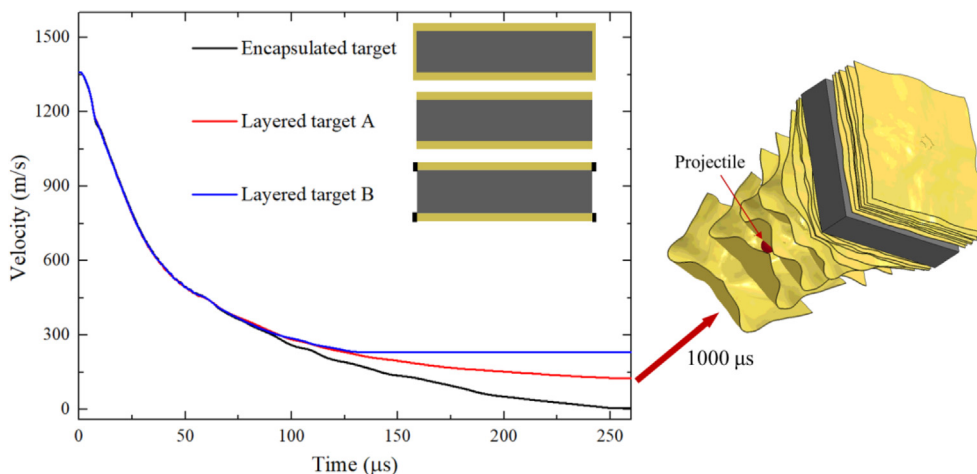


Fig. 13. Velocity histories of projectile for three targets at initial impact velocity of 1360 m/s.

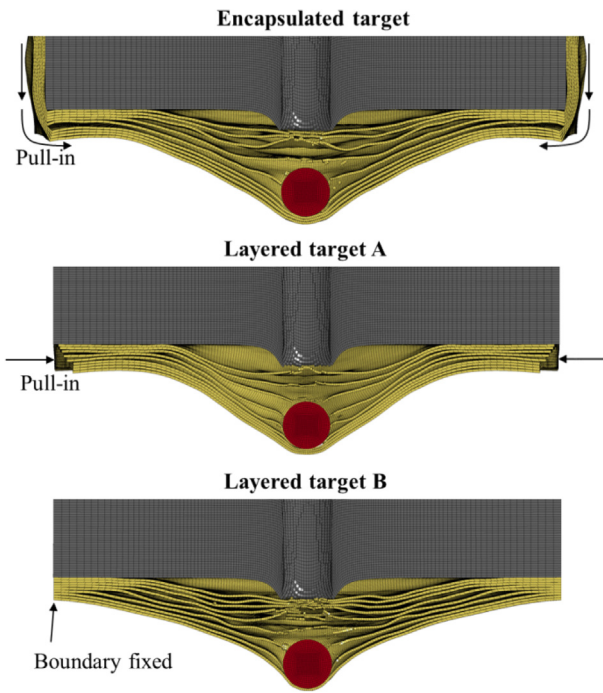


Fig. 14. Deformation and failure of rear laminate for three types of target at 125 μ s.

deflected like tight strings and hence would be penetrated more easily, reducing the penetration resistance. Therefore, encapsulating was the best choice for constructing a target with superior ballistic resistance.

4.2.3. Influences of impact velocity and lateral size

At last, how the impact velocity of the projectile and the lateral size of the target affected ballistic performance was calculated, and the results were presented in Fig. 15. When varying the lateral size of the composite structure, the thickness of both the Al plate and the laminate remained unchanged. With reference to Fig. 15(a), the benefits of encapsulating disappeared as the impact velocity exceeded 1540 m/s. This was mainly attributed to less stretching of the lateral swathing laminates at higher impact velocities. From Fig. 15(b) it was seen that the encapsulating effects was significant only for small targets, and there was only a 10% enhancement in ballistic limit for a 50 mm target. For layered target A, as the lateral size of Al plate was increased, the mass of the rear laminate increased and hence it became hard to be carried along with the projectile, leading to a continuous increase in ballistic limit. In contrast, as the lateral size was increased from 50 mm to 200 mm, the ballistic limit of layered target B increased from 1230 m/s to 1300 m/s; however, increasing further the lateral size did not improve the ballistic limit. The ballistic limit of the encapsulated target increased slightly with increasing lateral size and was nearly caught up by that of the layered target A; Fig. 15(b). Therefore, the lateral swathing laminates acting as a constrained boundary condition plays a major role for small targets and a minor role when the lateral size is sufficiently large.

5. Concluding remarks

A solid element continuum methodology with a simple composite model was proposed to simulate the ballistic behavior of UHMWPE composites. Two types of target, UHMWPE laminated plate and UHMWPE encapsulated aluminum structure, were modelled and validated against existing experimental ballistic results. The numerically calculated deformation features as well as failure modes agreed fairly well with those from experiments. Moreover, ballistic limit and residual velocity predictions were also in good agreement with experimental measurements. Therefore, the feasibility and validity of numerical model developed in the present study was established.

Further discussion of UHMWPE laminated plate found that:

1. The contact force between the projectile and the laminate was related to the local small deformation and failure in thicker laminates, which would be significantly reduced by the tensile relief wave reflected from the rear free face.
2. The perforation of laminated plate was controlled by the tensile stress at rear face, which would reach a maximum during the initial stage of bulge formation. In the subsequent membrane stretching stage, the tensile stress would be released by the pull-in from edges.

As the interface strength increased, the ballistic performance of laminate decreased and the failure mode changed to shear plugging.

For the UHMWPE encapsulated aluminum structure, it was found that:

1. The front laminate failed in compression without deflection deformation, while the rear laminate failed in tension with large deflection deformation.
2. During penetration, the lateral laminates would be stretched by the rear laminate. This in-plane stretching of the lateral laminates absorbed energy more effectively than the deflection of the rear laminates, providing the lateral laminates with the highest energy absorbing ability.

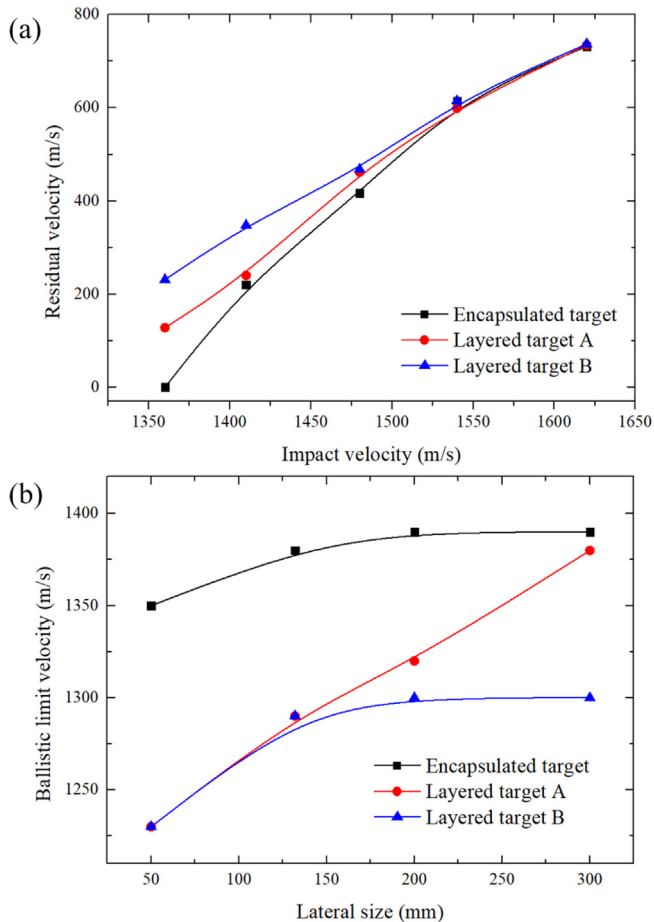


Fig. 15. Influences of (a) projectile impact velocity and (b) lateral size on ballistic limit of three different composite structures.

3. As the impact velocity and lateral dimensions increased, the benefits of the encapsulated aluminum structure disappeared, implying the role played by the lateral laminates became smaller.

CRedit authorship contribution statement

Rui Zhang: Methodology, Conceptualization, Writing - original draft. **Lu-Sheng Qiang:** Visualization, Data curation. **Bin Han:** Writing - review & editing, Formal analysis. **Zhen-Yu Zhao:** Software, Project administration. **Qian-Cheng Zhang:** Resources. **Chang-Ye Ni:** Writing - review & editing, Resources. **Tian Jian Lu:** Writing - review & editing, Supervision. : .

Declaration of Competing Interest

The authors declare that they have no known competing financial interests or personal relationships that could have appeared to influence the work reported in this paper.

Acknowledgments

The authors gratefully acknowledge the financial support by the National Natural Science Foundation of China (11972185, 11902148 and 11802221), the Open Fund of the State Key Laboratory of Mechanics and Control of Mechanical Structures (MCMS-I-0219K01 and MCMS-E-0219K02), the Natural Science Fund Project in Jiangsu Province of China (BK20190392), State Key Laboratory of Smart Manufacturing for Special Vehicles and Transmission System + GZ2019KF015.

Appendix A. Supplementary data

Supplementary data to this article can be found online at <https://doi.org/10.1016/j.compstruct.2020.112686>.

References

- Zhang TG, Satapathy SS, Vargas-Gonzalez LR, Walsh SM. Ballistic impact response of Ultra-High-Molecular-Weight Polyethylene (UHMWPE). *Compos Struct* 2015;133:191–201.
- Li D, Hou H, Chen C, Zhu X, Li M, Yi Q. Experimental study on the combined damage of multi-layered composite structures subjected to close-range explosion of simulated warheads. *Int J Impact Eng* 2018;114:133–46.
- Reddy TS, Reddy PRS, Madhu V. Response of E-glass/Epoxy and Dyneema® composite laminates subjected to low and high velocity impact. *Proc Eng* 2017;173:278–85.
- Karthikeyan K, Russell BP, Fleck NA, Wadley HNG, Deshpande VS. The effect of shear strength on the ballistic response of laminated composite plates. *Eur J Mech A Solids* 2013;42:35–53.
- Li X, Zhang X, Guo Y, Shim VPW, Yang J, Chai GB. Influence of fiber type on the impact response of titanium-based fiber-metal laminates. *Int J Impact Eng* 2018;114:32–42.
- Sapozhnikov SB, Kudryavtsev OA, Zhikharev MV. Fragment ballistic performance of homogenous and hybrid thermoplastic composites. *Int J Impact Eng* 2015;81:8–16.
- Nguyen LH, Ryan S, Cimpoeru SJ, Mouritz AP, Orifici AC. The Efficiency of Ultra-High Molecular Weight Polyethylene Composite Against Fragment Impact. *Exp Mech* 2015;56:595–605.
- Greenhalgh ES, Bloodworth VM, Iannucci L, Pope D. Fractographic observations on Dyneema® composites under ballistic impact. *Compos A Appl Sci Manuf* 2013;44:51–62.
- Attwood JP, Russell BP, Wadley HNG, Deshpande VS. Mechanisms of the penetration of ultra-high molecular weight polyethylene composite beams. *Int J Impact Eng* 2016;93:153–65.
- O'Masta MR, Crayton DH, Deshpande VS, Wadley HNG. Indentation of polyethylene laminates by a flat-bottomed cylindrical punch. *Compos A Appl Sci Manuf* 2016;80:138–47.
- Karthikeyan K, Russell BP. Polyethylene ballistic laminates: Failure mechanics and interface effect. *Mater Des* 2014;63:115–25.
- O'Masta MR, Crayton DH, Deshpande VS, Wadley HNG. Mechanisms of penetration in polyethylene reinforced cross-ply laminates. *Int J Impact Eng* 2015;86:249–64.
- Nguyen LH, Ryan S, Cimpoeru SJ, Mouritz AP, Orifici AC. The effect of target thickness on the ballistic performance of ultra high molecular weight polyethylene composite. *Int J Impact Eng* 2015;75:174–83.
- Attwood JP, Khaderi SN, Karthikeyan K, Fleck NA, O'Masta MR, Wadley HNG, et al. The out-of-plane compressive response of Dyneema® composites. *J Mech Phys Solids* 2014;70:200–26.
- Karthikeyan K, Russell BP, Fleck NA, O'Masta M, Wadley HNG, Deshpande VS. The soft impact response of composite laminate beams. *Int J Impact Eng* 2013;60:24–36.
- Shen Z, Hu D, Zhang Y, Cai Q, Han X. Continuous twice-impacts analysis of UHMWPE laminate fixed with bolted joints. *Int J Impact Eng* 2017;109:293–301.
- Tan VBC, Khoo KJL. Perforation of flexible laminates by projectiles of different geometry. *Int J Impact Eng* 2005;31:793–810.
- O'Masta MR, Deshpande VS, Wadley HNG. Mechanisms of projectile penetration in Dyneema® encapsulated aluminum structures. *Int J Impact Eng* 2014;74:16–35.
- O'Masta MR, Compton BG, Gamble EA, Zok FW, Deshpande VS, Wadley HNG. Ballistic impact response of an UHMWPE fiber reinforced laminate encasing of an aluminum-alumina hybrid panel. *Int J Impact Eng* 2015;86:131–44.
- Chocron S, Nicholls AE, Brill A, Malka A, Namir T, Havazelet D, et al. Modeling unidirectional composites by bundling fibers into strips with experimental determination of shear and compression properties at high pressures. *Compos Sci Technol* 2014;101:32–40.
- Lässig T, Nguyen L, May M, Riedel W, Heisserer U, van der Werff H, et al. A non-linear orthotropic hydrocode model for ultra-high molecular weight polyethylene in impact simulations. *Int J Impact Eng* 2015;75:110–22.
- Nguyen LH, Lässig TR, Ryan S, Riedel W, Mouritz AP, Orifici AC. A methodology for hydrocode analysis of ultra-high molecular weight polyethylene composite under ballistic impact. *Compos A Appl Sci Manuf* 2016;84:224–35.
- Hazzard MK, Trask RS, Heisserer U, Van Der Kamp M, Hallett SR. Finite element modelling of Dyneema® composites: From quasi-static rates to ballistic impact. *Compos A Appl Sci Manuf* 2018;115:31–45.
- Vila-Ortega J, Ridruejo A, Martínez-Hergueta F. Multiscale numerical optimisation of hybrid metal/nonwoven shields for ballistic protection. *Int J Impact Eng* 2020;138:103478.
- Liu W, Chen Z, Chen Z, Cheng X, Wang S. Influence of different back laminate layers on ballistic performance of ceramic composite armor. *Mater Des* 2015;87.
- Cai S, Liu J, Zhang P, Li C, Cheng Y. Dynamic response of sandwich panels with multi-layered aluminum foam/UHMWPE laminate cores under air blast loading. *Int J Impact Eng* 2020;138:103475.
- O'Masta MR, Deshpande VS, Wadley HNG. Defect controlled transverse compressive strength of polyethylene fiber laminates. *Int J Solids Struct* 2015;52:130–49.
- Sadighi M, Pärnänen T, Alderliesten RC, Sayeafabi M, Benedictus R. Experimental and numerical investigation of metal type and thickness effects on the impact resistance of fiber metal laminates. *Appl Compos Mater* 2011;19:545–59.
- Feli S, Asgari MR. Finite element simulation of ceramic/composite armor under ballistic impact. *Compos B Eng* 2011;42:771–80.
- Attwood JP, Fleck NA, Wadley HNG, Deshpande VS. The compressive response of ultra-high molecular weight polyethylene fibres and composites. *Int J Solids Struct* 2015;71:141–55.
- Huang W, Wang Y, Xia Y. Statistical dynamic tensile strength of UHMWPE-fibers. *Polymer* 2004;45:3729–34.
- Russell BP, Karthikeyan K, Deshpande VS, Fleck NA. The high strain rate response of Ultra High Molecular-weight Polyethylene: From fibre to laminate. *Int J Impact Eng* 2013;60:1–9.
- Hajjalizadeh F, Mashhadi MM. Investigation and numerical analysis of impulsive hydroforming of aluminum 6061-T6 tube. *J Manuf Processes* 2015;20:257–73.
- Wadley HNG, Dharmasena KP, O'Masta MR, Wetzel JJ. Impact response of aluminum corrugated core sandwich panels. *Int J Impact Eng* 2013;62:114–28.
- Meshi I, Amarilio I, Benes D, Haj-Ali R. Delamination behavior of UHMWPE soft layered composites. *Compos B Eng* 2016;98:166–75.
- Zhang Y, Liu T, Xu Z. Dynamic response of hybrid carbon fibre laminate beams under ballistic impact. *Compos Struct* 2019;210:409–20.
- Liu BG, Wadley HNG, Deshpande VS. Failure mechanism maps for ultra-high molecular weight polyethylene fibre composite beams impacted by blunt projectiles. *Int J Solids Struct* 2019;178–179:180–98.
- Lässig T, Bagusat F, Pfändler S, Gulde M, Heunoske D, Osterholz J, et al. Investigations on the spall and delamination behavior of UHMWPE composites. *Compos Struct* 2017;182:590–7.
- Zhu W, Huang G-y, Feng S-s, Stronge WJ. Conical nosed projectile perforation of polyethylene reinforced cross-ply laminates: Effect of fiber lateral displacement. *Int J Impact Eng* 2018;118:39–49.